LANGMUIR

Article

pubs.acs.org/Langmuir

Microporous Polymer Particles via Phase Inversion in Microfluidics: Impact of Nonsolvent Quality

Christiana E. Udoh, Valeria Garbin, and João T. Cabral*

Department of Chemical Engineering, Imperial College London, London SW7 2AZ, U.K.

Supporting Information

ABSTRACT: We investigate the impact of ternary phase behavior on the microstructure of porous polymer particles produced by solvent extraction of polymer solution droplets by a nonsolvent. Microfluidic devices fabricated by frontal photopolymerization are employed to produce monodisperse polymer (P)/solvent (S) droplets suspended in a carrier (C) phase before inducing solvent extraction by precipitation in a nonsolvent (NS) bath. Model systems of sodium poly(styrenesulfonate) (P), water (S), hexadecane (C), and either methyl ethyl ketone (MEK) or ethyl acetate (EA) as NS are selected. Extraction across the liquid−liquid interface results in a decrease in the droplet radius and also an ingress of nonsolvent, leading to droplet phase demixing and coarsening. As the concentration of the polymer-rich phase increases, droplet shrinkage and solvent exchange slow down and eventually cease, resulting in microporous polymer particles (of radius ≃50−200 μm) with a smooth surface. The internal structure of these capsules, with pore sizes of ≃1−100 μm, is found to be controlled by polymer solution thermodynamics and the extraction pathway. The ternary phase diagrams are measured by turbidimetry, and the kinetics of phase separation is estimated by stopped-flow small-angle neutron scattering. The higher solubility of water in MEK results in faster particle-formation kinetics than in EA. Surprisingly, however, the lower polymer miscibility with EA/water results in a deeper quench inside the phase boundary and small phase sizes, thus yielding particles with small pores (of narrow distribution). The effects of droplet size, polymer content, and nonsolvent quality provide comprehensive insight into porous particle and capsule formation by phase inversion, with a range of practical applications.

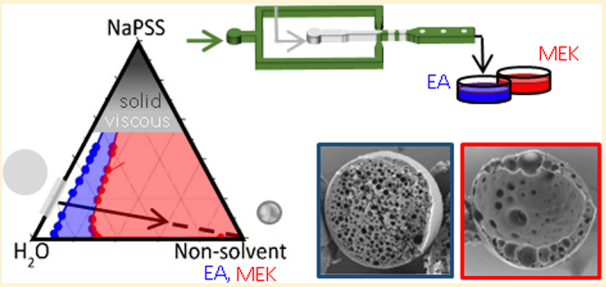

INTRODUCTION

Polymer particles are central to a range of industries, including personal care, coatings, formulations, pharmaceuticals, and biomedical.[1] The function and performance of polymer particles in different applications can be precisely controlled through the particle microstructure. Each application requires particles with unique microstructure. For instance, the polymer particle size and morphology have been shown to be critical for drug release rate kinetics and payload.[2,3] Polymer particles with suitable powder flow and aerodynamic properties are required for pharmaceutics, typically formed by spray drying.[4]

Polymer particles are typically formed by either the polymerization of monomers (via a range of synthesis routes) or by the dispersion of polymers (followed by solidification through solvent extraction or temperature change), within a desired geometry, set by the associated emulsification, suspension, dispersion, or precipitation processes.[5] For polymer particles formed by solvent extraction, polymer droplets are first produced by emulsification, acoustic excitation, dipped inkjet injection, or microfluidics[6−9] and then concentrated by subsequent extraction of the droplet solvent with an external solvent or by spray drying. Despite the significant developments in the fabrication of polymer particles with precise size and shape control,[10] a detailed understanding of the mechanism and kinetics that control the microstructure of polymer particles remains elusive.

We have previously demonstrated the formation of microporous polymer particles by solvent extraction in microfluidics.[8] Mono- and bidisperse polymer solution droplets were produced with a standard T-junction, convected with an inert carrier phase, and precipitated at a flow-focusing junction with a nonsolvent. For this demonstration, a sodium poly(styrenesulfonate)/water mixture was employed as the droplet phase, hexadecane was employed as the carrier, and MEK was employed as the precipitation phase. The kinetics of particle formation in the 10−120 μm range were found to be ∼10−60 s, and because of the much faster droplet production rates, we have opted to carry out extraction by an ex-situ precipitation stage. The approach requires the precipitation phase to be a nonsolvent for the polymer, such that precipitation occurs, but miscible with the polymer solvent such that solvent displacement and extraction take place. The carrier solvent phase, responsible for droplet formation, must thus also be miscible with the precipitation nonsolvent but now immiscible with the polymer solution. A significant advantage of our microfluidic

Received: May 11, 2016
Revised: June 28, 2016
Published: July 22, 2016

DOI: 10.1021/acs.langmuir.6b01799
Langmuir 2016, 32, 8131−8140

approach is that it does not require the use of porogens,[11] external fields (e.g., temperature or UV light exposure), or synthetic routes. Furthermore, it offers the potential of single-stage encapsulation and micropore formation.

Our approach is reminiscent, albeit distinct, of two methodologies employed in the preparation of polymer nanoparticles.[12,13] Polymer nanoprecipitation[14] involves the displacement of solvent with a nonsolvent, carried out under turbulent flow conditions, optimized in opposing[15] and coaxial[16] jet mixers, with typical mixing times of ∼10 ms. By contrast, our approach takes place at low Reynolds number, involving an additional phase (the droplet carrier), and particle size and precipitation times are approximately 1000 times larger. The porous internal structure of these particles, can be thought as templated[12] by the demixed polymer solution, whose coarsening is then kinetically arrested by further solvent extraction.

In this article, we examine the role of the ternary phase behavior of the polymer/solvent/nonsolvent in the design of porous polymer particles and comparatively evaluate the impact of nonsolvent, polymer concentration and droplet size on particle microstructure. We expect this systematic examination to provide insight into the governing parameters for porous particle formation by solvent extraction.

EXPERIMENTAL SECTION

System. Sodium poly(styrenesulfonate) (NaPSS) with an average molecular weight of 70 000 g/mol, methyl ethyl ketone (puriss. p.a, ACS reagent, ≥99.5% purity), *n*-hexadecane (ReagentPlus, ≥99%), toluene, octadecyltrichlorosilane (OTS), and sorbitane mono-oleate (span80) were obtained from Sigma-Aldrich. Ethyl acetate (HiperSolv Chromanorm, ≥99.8% purity), acetone, ethanol, and isopropyl alcohol (all Analar, Normapur) were obtained from VWR International. NOA 81 (thiolene-based prepolymer) was obtained from Norland Products, and deionized water was obtained from a Centra ELGA filtration system. All reagents were used as received.

Phase Mapping and Viscosity. The ternary phase diagrams of polymer/solvent/nonsolvent were estimated by turbidity measurements to determine the thermodynamic compositional stability of both systems. Cloud-point curves for NaPSS/H_2O/MEK and NaPSS/H_2O/EA systems were obtained by measuring the onset of turbidity by visual inspection and optical microscopy. Polymer solutions (40 mL) were prepared on a mass (g) per total volume (mL) basis and are indicated in wt % (i.e., 0.01 g/mL = 1 wt %). Concentrations ranging from 1 to 45 wt % were prepared, and nonsolvent was added to 3 mL of polymer solution in 0.1 mL increments and agitated until turbid. In total, over 100 samples of different compositions were employed to locate the phase boundaries with ±5% precision. The viscosity of polymer solutions with concentration from 1 to 45 wt % was measured using a Brookfield DV-I Prime viscometer fitted with an ultralow adapter. The spindle speed was varied between 4 and 100 rpm depending on the polymer solution concentration. All samples studied exhibit Newtonian behavior in this range. The overlap concentration, c^*, of NaPSS is estimated from the reciprocal of the intrinsic viscosity $[\eta]$ as ∼2.38 wt %. By assuming $\eta_{sp} = [\eta]c$ in the dilute, where η_{sp} is the specific viscosity and c the polymer concentration, the intrinsic viscosity is obtained from a linear extrapolation of the reduced viscosity to zero concentration.[17]

Small-Angle Neutron Scattering (SANS). Static SANS experiments for 2.5 and 5.0 wt % NaPSS/D_2O solutions were carried out at the D22 spectrometer of the Institut Laue-Langevin (Grenoble, France) with incident wavelength λ = 6 Å, sample−detector distances of 1.4 and 5.0 m, and collimation values of 2.8 and 5.6 m. The accessible q range (where $q = (4\pi/\lambda)\sin(\theta/2)$) is therefore 0.013−0.608 $Å^{-1}$. The stopped-flow SANS experiments were also carried out at D22 with a sample−detector distance of 17.6 m and a collimation of 17.6 m, yielding a q range of 0.0022−0.055 $Å^{-1}$ to probe demixing. Measurements were carried out with 1 mm quartz cells (Hellma, Germany). For stopped-flow experiments, NaPSS/D_2O solution and nonsolvent were injected simultaneously at a flow rate of 3 mL/s and a volume ratio of 2:1. NaPSS/D_2O solutions with concentrations of 5.0 and 10.0 wt % were used. Total measurement times for static and stopped-flow SANS were 600 and 420 s, respectively. The data was extracted using LAMP and reduced and calibrated using GRASP.

Microfluidics and Extraction. A microfluidic device with a flow-focusing junction was fabricated by the frontal photopolymerization (FPP) of a thiolene optical adhesive (Norland NOA 81) using a previously reported procedure.[18,19] The microchannels were 100 μm deep and 650 μm wide, with a focusing constriction of 300 μm. Channel surfaces were rendered hydrophobic by treating with a 10 wt % solution of OTS in toluene for 1 h, followed by 24 h in a convection oven at 110 °C. The device was mounted on an *XY* microscope stage (Prior Scientific). Inlets were connected with silicone tubing to 10 mL syringes mounted on syringe pumps (Braintree BS-8000), and the outlet tube was connected to the nonsolvent bath. The dispersed phase was the polymer solution, and the continuous phase was hexadecane with 2−5 v/v% Span80. A refractive index mismatch between the droplet and nonsolvent allows for droplet edge detection and image thresholding followed by droplet shape and size analysis, from which the droplet radius was obtained. The initial droplet radius was varied by changing the flow rate of the continuous phase, F_c, within 50 to 90 μL/min while the dispersed-phase flow rate, F_d, was kept constant at 10 μL/min, corresponding to a Reynolds number ($Re = \rho UL/\eta$, where ρ is the density, U is the flow velocity, L is the characteristic length, and η is the viscosity) of between 0.17 and 0.3. The polymer solution droplets, suspended in hexadecane, were then precipitated into an external nonsolvent bath with a large excess volume (20 mL).

Particle Characterization. The droplet shrinkage and evolution of internal morphology during solvent extraction were monitored using an upright reflection microscope (Olympus BX41M) and CCD camera (Allied Technologies, Mantra F-145, 1392 × 1040 pixels, 20 fps). The internal structure of the final polymer particles was observed by scanning electron microscopy (SEM) with a tabletop TM-1000 (Hitachi) microscope. Particles were dried for 24 h, sectioned or crushed between glass plates, and coated with gold before SEM imaging. The overall particle porosity and pore size distribution were extracted through image analysis using ImageJ.

RESULTS AND DISCUSSION

Prior to particle formation experiments by droplet extraction, the mixture thermodynamics of NaPSS/H_2O with both MEK and EA were determined experimentally by turbidimetry. The resulting polymer/solvent/nonsolvent ternary phase diagrams, on a volume basis, are shown in Figure 1a. The one-phase region for the NaPSS/H_2O/EA system is found to be comparatively smaller than that of the NaPSS/H_2O/MEK system, indicating that phase separation occurs at lower nonsolvent concentrations for the EA system. In terms of the binary solvent mixtures, EA has a lower solubility in water, approximately 9 v/v%, than MEK in water, estimated at 31 v/v %, and the phase stability line roughly follows these solvent/nonsolvent ratios.

The experimental setup for microfluidic droplet formation and ex situ precipitation is shown in Figure 1b. The carrier phase (C), hexadecane in our case, must be fully miscible with nonsolvents (NS) MEK and EA but immiscible with the solvent (S). With the device geometry and operation, it plays a significant role in setting the droplet size and preventing coalescence.

The immersion of the polymer solution droplets in the nonsolvent triggers the solvent extraction (sometimes referred to as evaporation), and microporous particles are formed. We expect the process to evolve as follows: the rapid mixing of C

DOI: 10.1021/acs.langmuir.6b01799
Langmuir 2016, 32, 8131−8140

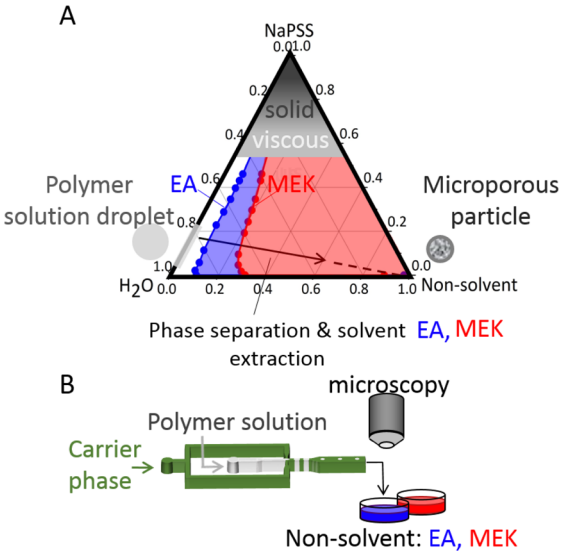

Figure 1. (A) Experimentally measured phase diagrams for NaPSS/H_2O/EA and NaPSS/H_2O/MEK, indicating the two-phase region and the viscous to solid polymer-rich compositions. The arrow indicates the overall composition trajectory of the NaPSS/H_2O solution droplet immersed in excess pure nonsolvent. Microporous particles, with a smooth surface, are generated by simultaneous phase separation and solvent extraction. (B) Schematic of the experimental setup, showing droplet formation in microfluidics assisted by a carrier phase (hexadecane), followed by ex situ precipitation in a nonsolvent bath.

into the NS bath (in great volume excess) brings the NS into contact with the droplet interface, enabling S/NS exchange; water (S) is extracted from the polymer solution droplet, increasing both the polymer and nonsolvent concentrations within the droplet, until the phase boundaries are reached. At this point, phase separation within the droplet begins and continues over time as further extraction takes place. Eventually, kinetic arrest is expected when the polymer concentration in one phase within the droplet becomes sufficiently high, resulting in the formation of a solid particle.

The solvent interdiffusion process at the droplet interface is thus analogous to the phase inversion in membrane formation.[20,21] The kinetics of polymer particle formation should depend on the mutual diffusion coefficient between the solvent and nonsolvent, the mixture phase diagram, droplet size, and solution ("dope") viscosity in a complex interplay of thermodynamics, mass transfer, demixing, and kinetic arrest.

For this study, we employ polymer solution concentrations ranging from 1 to 10 wt %. Our hypothesis is that by shifting the phase boundaries of the polymer/solvent/nonsolvent system, precise control can be achieved in the internal structure of the resulting polymer particles. For instance, one might expect the EA system to yield particles with larger internal voids because the system would cross the phase boundaries earlier during the extraction process and thus coarsen for a comparatively longer time.

We first report on two sets of SANS experiments: static scattering to characterize NaPSS/D_2O solutions and stopped flow to investigate the mechanism and relative kinetics of phase separation induced by EA or MEK. The stopped-flow experiment is similar to the flash nanoprecipitation process,[22] employed in the formation of multifunctional polymer particles, by the rapid injection of polymer solution and nonsolvent.

Figure 2a shows the experimental setup for stopped-flow SANS, and Figure 2b shows the (quiescent) radially averaged coherent scattering for the semidilute solutions with 2.5 and 5 wt % NaPSS/D_2O. The structure factor, $S(q)$, of semidilute salt-free polyelectrolyte solutions is expected to exhibit a correlation peak[23,24] attributed to hard-sphere-like repulsion generated by the cloud of counterions surrounding the polyion, preventing the overlap of correlation blobs.[25] Our data does not show a peak, as expected for polyelectrolyte solutions in the presence of salt, that screens the Coulomb interactions between charged monomers.[26−28] Indeed, we estimate the salt to monomer ratio to be approximately 1:3 to 1:4 in our commercial NaPSS system. Fits of the static SANS data to the Ornstein−Zernike model with an exponent of 2 are poor, suggesting that the polymer conformation cannot be

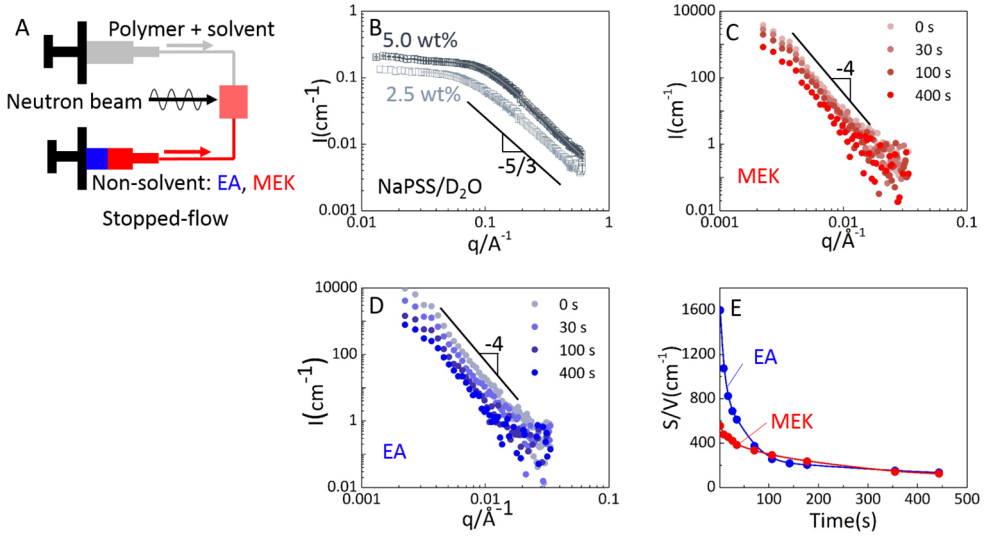

Figure 2. (A) Schematic of the stopped-flow SANS experiment with NaPSS/D_2O and MEK (or EA) solutions injected in a 2:1 ratio at a flow rate of 3 mL/s. (B) Static 1D coherent SANS profile of NaPSS/D_2O solutions with 2.5 and 5 wt % polymer mass fractions. Stopped-flow experimental results with (C) nonsolvent MEK and (D) EA, with 5 wt % NaPSS/D_2O. The data is interpreted according to eq 1, whose intercept S/V is plotted in (E). The lines are guides to the eye.

DOI: 10.1021/acs.langmuir.6b01799
Langmuir 2016, 32, 8131−8140

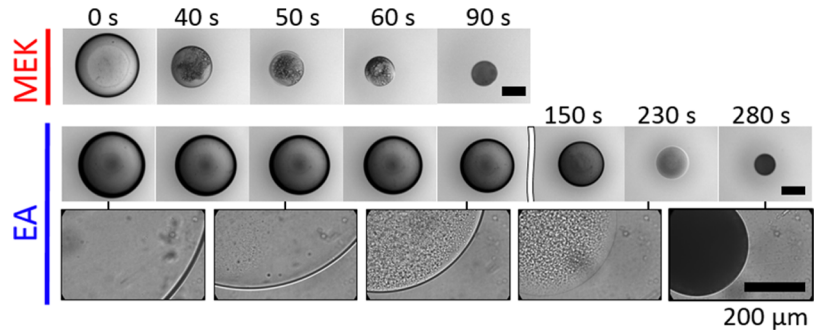

Figure 3. Representative time series of polymer solution droplet extraction and demixing with nonsolvents MEK (top row) and EA (bottom rows). Images were obtained by reflection optical microscopy. The concentration of the NaPSS/H_2O solution was 1.0 wt %, and the initial droplet radius was 100 μm. Demixing is visible in both series, albeit at a smaller scale in EA and over longer time scales.

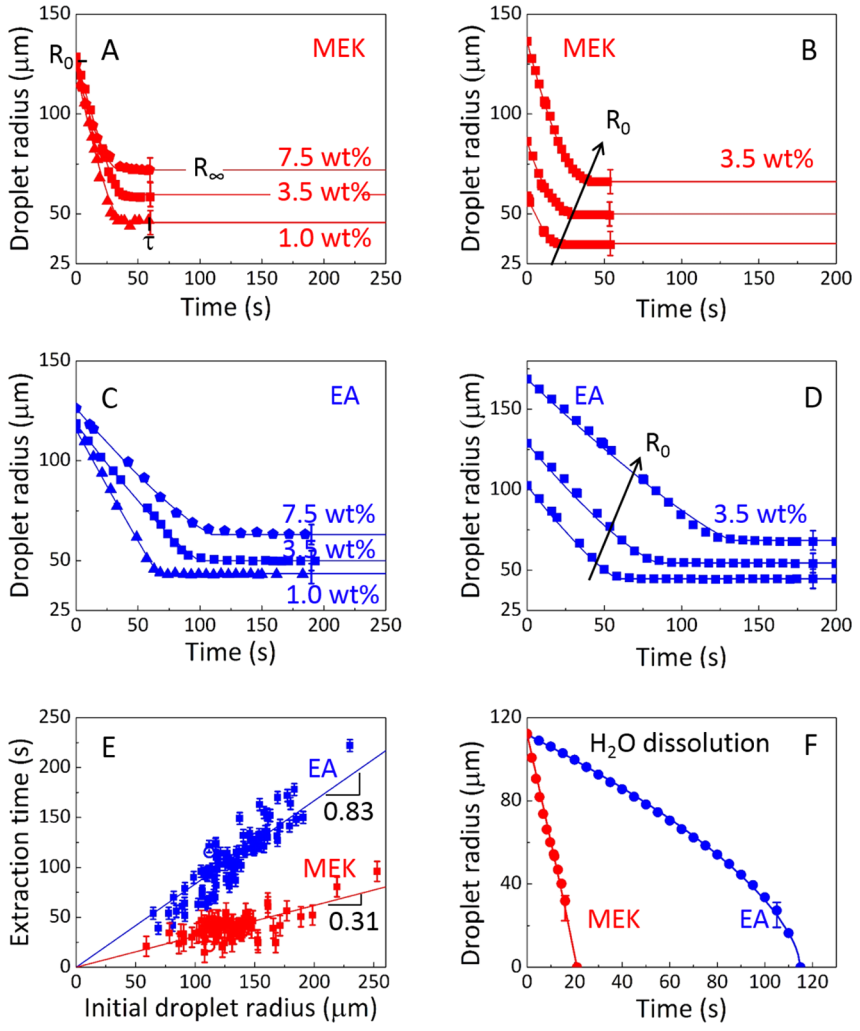

Figure 4. Optical microscopy image analysis of droplet extraction kinetics. (A) Evolution of droplet radius over time for NaPSS solutions of different concentrations extracted in MEK; the initial and final droplet radii R_0 and R_∞ and the extraction time τ are indicated. (B) Effect of initial droplet radius R_0 on particle formation kinetics. (C, D) Corresponding data for nonsolvent EA. (E) Dependence of extraction time τ on initial droplet radius R_0 for all NaPSS concentrations studied for nonsolvents EA and MEK. Dissolution times for a pure H_2O droplet of radius 110 μm in EA and MEK are shown as open circles. (F) Reference H_2O droplet dissolution kinetics in MEK and EA. Lines shown in A–D and F are fits of eq 2 to the extraction data.

approximated by a Gaussian chain in a θ solvent. Instead, we observe a high q scaling exponent of approximately 5/3, corresponding to a polymer in a good solvent,[29] and a subtle polyelectrolyte shoulder for the highest polymer concentration.

Figure 2c,d shows the time-resolved scattering profiles for NaPSS/D_2O/MEK and NaPSS/D_2O/EA mixtures during phase separation and precipitation. For both mixtures, we observe demixing features: strong forward scattering, a q^{-4} power law corresponding to sharp interfaces, and a decrease in

DOI: 10.1021/acs.langmuir.6b01799
Langmuir 2016, 32, 8131–8140

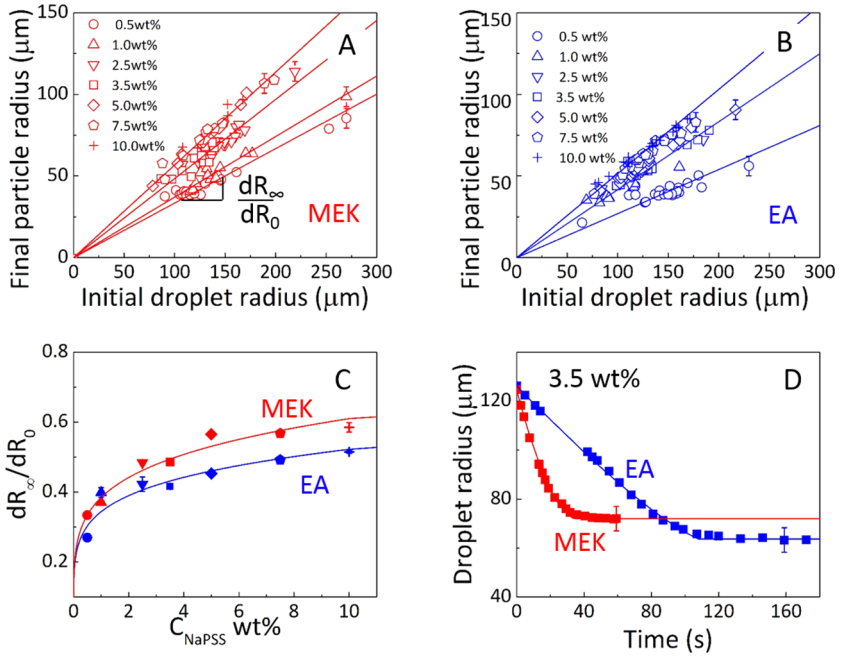

Figure 5. Dependence of the final particle radius R_∞ on the initial droplet radius for nonsolvents (A) MEK and (B) EA at all NaPSS concentrations studied. (C) Slope dR_∞/dR_0 obtained from A and B for the two nonsolvents as a function of NaPSS concentration. (D) Comparative extraction kinetics of a 3.5 wt % NaPSS/H_2O droplet of the same initial radius (125 μm) after immersion in MEK and EA; the lines shown are fits of eq 2 to the extraction data.

overall intensity with time. No spinodal peak or spherelike form factor is clearly found in the data, which could be due to the polydispersity of phase sizes and integration over long times compared to demixing and coarsening. Instead, a Porod model[30] is fit to the stopped-flow data

$$I = \frac{2\pi\Delta\rho S/V}{q^4} + I_{\text{inc}} \tag{1}$$

where $\Delta\rho = (b_{\text{solute}}/v_{\text{solute}} - b_{\text{solvent}}/v_{\text{solvent}})^2$ is the contrast factor, S/V is the surface to volume ratio of the sample, and I_{inc} is the incoherent intensity.

After the subtraction of background intensity, free exponent fits of the Porod model to the stopped-flow data result in values of between 3.85 and 4.06. To allow for the robust comparison of both systems, we fix the Porod exponent at 4 and fit the time-dependent intensity to extract the change in the surface to volume ratio of the mixtures with time. The change in S/V with time for both systems is shown in Figure 2e. We find that the initial S/V for the NaPSS/D_2O/EA mixture is 4 times higher than that of the MEK system and the decay rate of S/V for the EA mixture during phase separation is higher than that for the MEK mixture. The higher surface to volume ratio and decay rate for the EA mixture could be attributed to the presence of a larger interface area and a higher coarsening rate, respectively, relative to the MEK mixture as expected from the phase diagram (Figure 1a) because EA is a poorer nonsolvent for the system.

With the above observations in mind, we then investigate systematically the particle-formation mechanism and kinetics with a combination of microfluidic extraction experiments and particle characterization.

Optical micrographs of droplet kinetics during solvent extraction are shown in Figure 3 for NaPSS/H_2O droplets of 1 wt % polymer concentration immersed in MEK and EA nonsolvents. Immersion in MEK is found to result in particle formation considerably more rapidly than in EA. The optical images for either MEK or EA extraction show clear demixing within droplets during size reduction. However, the scale of phase separation of EA-immersed droplets appears to be measurably smaller than that of those extracted in MEK, where large internal droplets are clearly seen and coarsen rapidly. By following the kinetic pathway to particle formation in Figure 3 (and Supporting Information movies S1 and S2), a few key observations can be made. (1) The smooth polymer outer skin appears within the very last stages of particle formation. (2) The internal porosity corresponds to the polymer-poor demixed phase within the droplet. Although the limited spatial resolution of optical microscopy cannot discriminate between spinodal decomposition or nucleation and growth mechanisms, we note that demixing first appears close to the liquid–liquid interface, with isolated and sparse droplets, and then evolves into rather homogeneous cloudiness, as detailed in Supporting Information Figure S1. This suggests that solvent/nonsolvent concentration gradients are significant during extraction. However, (3) substantial droplet recirculation occurs alongside, indicating that internal convection plays a significant role, together with diffusion across the liquid–liquid interface. (4) The outer droplet surface always appears to be smooth, indicating that the interfacial tension is sufficiently large to yield a spherical surface, despite the internally heterogeneous structure of the droplet. Finally, both processes result in polymer particles with smooth outer surfaces during the solidification stage by kinetic arrest.

Close inspection reveals that the MEK-extracted particles are larger and form more rapidly than those extracted with EA, starting from polymer solution droplets of identical size and composition. These results are somewhat surprising because EA is the poorer solvent, which led us to investigate the relative effects of droplet size, polymer concentration, and nonsolvent quality.

DOI: 10.1021/acs.langmuir.6b01799
Langmuir 2016, 32, 8131–8140

For both nonsolvents, we investigate a wide range of concentrations from 1 to 10 wt % with a specific viscosity range of 0.4 to 4 mPa·s. Droplet shrinkage can be described by an empirical relation for the droplet radius

$$R(t) = (R_0 - R_\infty)\left(1 - \frac{t}{\tau}\right)^{\alpha} + R_\infty \quad (2)$$

where R_0 is the initial droplet radius, R_∞ is the (final) particle radius, τ is the extraction time (when R ceases to change), and α is a non-Fickian parameter, introduced previously.[8] Figure 4a,c shows the dependence of final particle size R_∞ on polymer concentration for both nonsolvents, fitted to eq 2. As expected, R_∞ increases with polymer concentration for droplets of the same initial size R_0. The dependence of R_∞ on R_0 for both nonsolvents is shown in Figure 4b,d. Interestingly, however, the dependence of the extraction time τ on R_0 for both nonsolvents is markedly different, as shown in Figure 4e. Particle formation in MEK occurs statistically 3 times faster than in EA. A dependence of τ on polymer concentration cannot be resolved within the measurement uncertainty. For particle formation in MEK, we obtain α values ranging from 1.0 ± 0.1 to 2.3 ± 0.3 for the range of polymer concentrations studied, in good agreement with previous observations.[8] By contrast, the slower particle formation with nonsolvent EA yields $\alpha \approx 1.2 \pm 0.2$ at all concentrations.

For comparison, the dissolution kinetics of pure H_2O droplets in both nonsolvents is shown in Figure 4f and also fitted to eq 2. This experiment enables us to compare pure water extraction and directly measure the diffusion kinetics across the droplet interface in the absence of polymer. For droplets with the same initial radius (110 μm shown here), dissolution in EA is approximately 3−5 times slower than in MEK. This ratio of time scales correlates favorably with the measured solubility of water in EA and MEK, approximately 3 and 11 v/v%, respectively. The slower kinetics of pure water dissolution in EA is compatible with the longer times observed for particle formation by EA extraction with an average ratio of 3. We find that for pure water dissolution in MEK and EA, α = 0.92 ± 0.05 and 0.6 ± 0.1, respectively. These results are in qualitative agreement with the expected impact of solute solubility on dissolution profile.[31]

The correlations plotted in Figures 4e and 5a−c compile parameters obtained for best fits for individual extraction $R(t)$ data sets for various droplet sizes, polymer concentrations, and nonsolvents EA and MEK. Given some scatter in the data, we validate the predictive nature of such correlations by comparing best fits (to a particular data set) to ensemble fits (calculated from the trendlines describing all data) in Supporting Information Figure S4. Representative measurements deviating the most from the trendline are selected, showing that the model yields a good description of all data. The uncertainties in Figure 4e are likely due to droplet crowding during particle formation, concentration gradients, and carrier phase removal and are associated with the estimation of initial time t = 0 and size R_0. For the droplet with radius 110 μm, we find that particle formation and water dissolution times are similar. We show the H_2O dissolution times for 110 μm droplets in MEK and EA as open circles in Figure 4e, in good agreement with their polymer solution counterparts. For the range of polymer concentrations and droplet sizes investigated, it therefore appears that the kinetics of particle formation are largely governed by water extraction.

In Figure 5a,b, we show that, for both nonsolvents, the dependence of the final particle size on the initial droplet size remains linear for all the polymer concentrations investigated, with slopes plotted in Figure 5c. For all concentrations and initial sizes investigated, we find that polymer particles formed in EA are 10−20% smaller than particles formed in MEK, as shown in Figure 5d for a 3.5 wt % polymer droplet of radius 125 μm. We next seek to reconcile this finding with the fact that EA is a poorer nonsolvent for this system.

SEM is employed to investigate the internal porous structure of the resulting polymer particles. For both nonsolvents, particles have smooth outer shells as shown in Figure 6a,e but

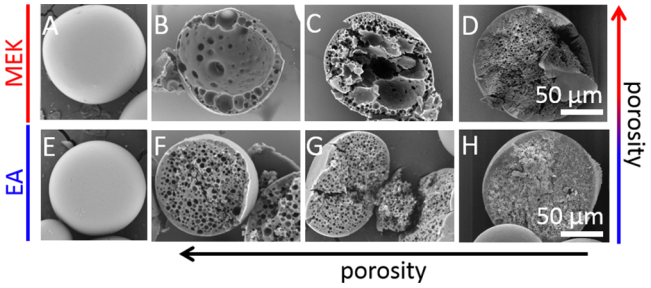

Figure 6. SEM micrographs of the final polymer particles obtained by extraction in MEK and EA. Panels A and E show the external (smooth) surface, and the remaining panels show the cross-section of particles. Particles extracted with MEK are visibly larger (approximately 20%) and more porous than those obtained with EA. (A, C, E, G) $C_{NaPSS,t=0}$ = 3.5 wt %, (B, F) $C_{NaPSS,t=0}$ = 1.0 wt %, and (D, H) $C_{NaPSS,t=0}$ = 10 wt %.

exhibit different internal morphology and porosity (defined as pore volume/total volume). Figure 6b−d shows the internal morphology for particles extracted with MEK and initial polymer concentrations of 1, 3.5, and 10 wt %, respectively. Droplets with a 1 wt % polymer content yield particles with large pores and thin shells. With increasing concentration, the pore size decreases and the pore density increases. We also observe an increase in the shell thickness (examined in Figure SI2). Replacing EA as a nonsolvent, we observe a remarkable difference in porosity as shown in Figure 6f−h. At low polymer concentration (1 wt %), the average pore size is 4 μm with a narrow distribution, in sharp contrast to the broad distribution and large pore size (with diameters as large as 60 μm) observed for particles formed using MEK as a nonsolvent. Despite the difference in porosity, the trend of decreasing porosity with increasing polymer concentration remains.

We compare the pore size distribution for particles produced using both nonsolvents in Figure 7a,b. With increasing polymer concentration, the standard deviation of the distribution and the average pore diameter decrease. Figure 7c shows the dependence of porosity on initial polymer concentration for both nonsolvents, overall establishing the lower porosity of EA-extracted particles, observed in the selected SEM micrographs in Figure 6.

We next consider the possibility of tuning the nonsolvent quality by investigating droplet immersion in solvent/nonsolvent mixtures. The nonsolvent strength is adjusted by dilution with water. Because the solubility of water in MEK is low (approximately 11 v/v %), the accessible composition window is rather small. Nevertheless, we evaluate droplet extraction by varying the MEK/H_2O composition and find this approach to be effective in controlling particle shell thickness

DOI: 10.1021/acs.langmuir.6b01799
Langmuir 2016, 32, 8131−8140

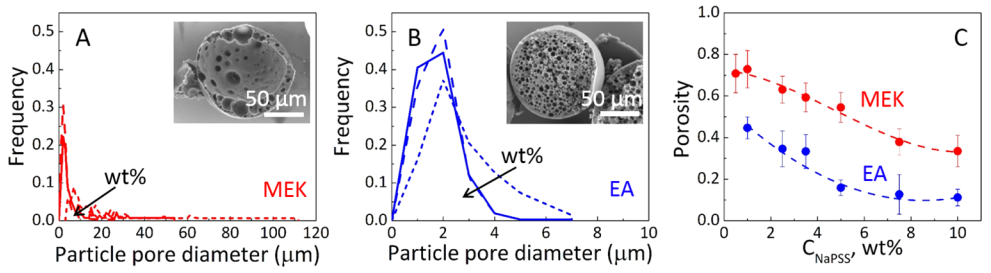

Figure 7. Internal pore size distribution of particles extracted in (A) MEK and (B) EA from droplets of 1 wt % (short dashes), 3.5 wt % (solid line), and 7.5 (dashed line) wt % NaPSS/H_2O solutions. The inset shows a representative SEM image (1 wt %). (C) Estimated porosity as a function of NaPSS concentration for the two nonsolvents.

and porosity. Droplets of 2.5 wt % polymer content and various diameters are extracted. We use a range of H_2O/MEK solutions with ratios 0.015/0.985, 0.025/0.975, 0.05/0.95, 0.06/0.94, and 0.07/0.93 and find that polymer particles are formed with H_2O/MEK ratios of 0.015/0.985 and 0.025/0.975 only. At higher H_2O content, droplet phase separation and coarsening occur, but solid particles are not formed, instead yielding viscous and tacky polymer droplets within the nonsolvent bath (Supporting Information Figure S2). When allowed to dry in ambient air, the viscous droplets dry further and eventually solidify. Figure 8a shows the compositions of diluted

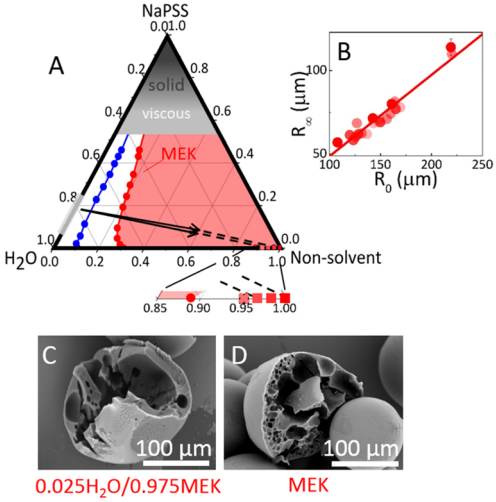

Figure 8. Effect of nonsolvent MEK dilution with H_2O in particle porosity. (A) Ternary phase diagram indicating extraction to pure MEK and MEK/H_2O (i.e., decreasing nonsolvent quality) up to 5% v/v H_2O. (B) The dependence of R_∞ on R_0 appears insensitive to the various H_2O/MEK ratios (up to 5% v/v). SEM micrographs for 2.5 wt % NaPSS/H_2O droplets extracted in (C) 2.5 v/v% H_2O/MEK and (D) pure MEK, revealing a larger porosity of the former.

nonsolvent mixtures on the ternary diagram. We mark the nonsolvent composition where solid particles form with a red square but otherwise with a cross, and we mark the H_2O miscibility in MEK with a circle.

Figure 8b shows that the nonsolvent quality, in this narrow composition range, does not seem to affect the final particle size and that the linear dependence between final particle size and initial droplet size is retained. However, with dilution of the nonsolvent, we observe an increase in the porosity of polymer particles and the thickness of the polymer shell. Figure 8c,d shows SEM micrographs of particles formed using H_2O/MEK solution with ratios 0.025/0.975 and 0.002/0.998, respectively. We find that the extraction time in the H_2O/MEK nonsolvent with ratio 0.025/0.975 is double the extraction time in the neat MEK nonsolvent. We therefore interpret these results as being due to the smaller composition gradient across the liquid interface and the delay in particle solidification, which allows longer time scales for coarsening and thus results in a core–shell structure with thicker outer shells.[32]

On the basis of our findings, we next seek to rationalize the mechanisms and kinetics of droplet-to-particle formation and its relation to nonsolvent thermodynamics. Figure 9 summarizes the physical picture proposed. In general, the immersion of the polymer solution droplet in the nonsolvent results in droplet shrinkage by solvent removal and thus an increase in the polymer concentration within the droplet. This process alone, corresponding to the side of the ternary diagram connecting H_2O and NaPSS, would not result in phase separation and microporosity. Solvent extraction is accompanied by the ingress of nonsolvent into the droplet, moving the droplet composition into the two-phase region, thus resulting in demixing. Phase separation evolves by coarsening of the demixed droplet morphology, accompanied by internal flow recirculation. As extraction proceeds, the polymer concentration in the polymer-rich phase increases further, causing a cascade of steps along the phase boundary. Eventually, the morphology within the droplet is kinetically arrested as the viscosity increases toward the glassy phase and the droplet solidifies into a particle. Figure 9e shows the experimentally measured viscosity of our system as the polymer concentration increases, in good agreement with the de Gennes scaling predictions for polyelectrolyte solutions in the dilute, semidilute unentangled, and concentrated regimes.[33] Dehydration of the polymer-rich phase is expected to yield approximately 80 wt % polymer content, as estimated by mass and volume conservation. The particle skin is formed from the polymer-rich phase, resulting in a smooth, spherical surface due to the interfacial energy minimization. This kinetic arrest traps a solvent-rich phase and thus yields the pores or voids observed under SEM. This pathway is depicted on the ternary diagram in Figure 9a–c and illustrated in Figure 9d.

■ CONCLUSIONS

We investigated the effect of polymer solution thermodynamics in particle formation via microfluidic solvent extraction by comparing two nonsolvents (EA and MEK) in the extraction of a polymer/solvent (NaPSS/H_2O) system. A carrier phase (hexadecane) is immiscible with the solvent but fully miscible with the nonsolvents, assisting in the formation of well-defined droplets in microfluidics. A range of process parameters are systematically investigated, namely, the size of the initial

DOI: 10.1021/acs.langmuir.6b01799
Langmuir 2016, 32, 8131–8140

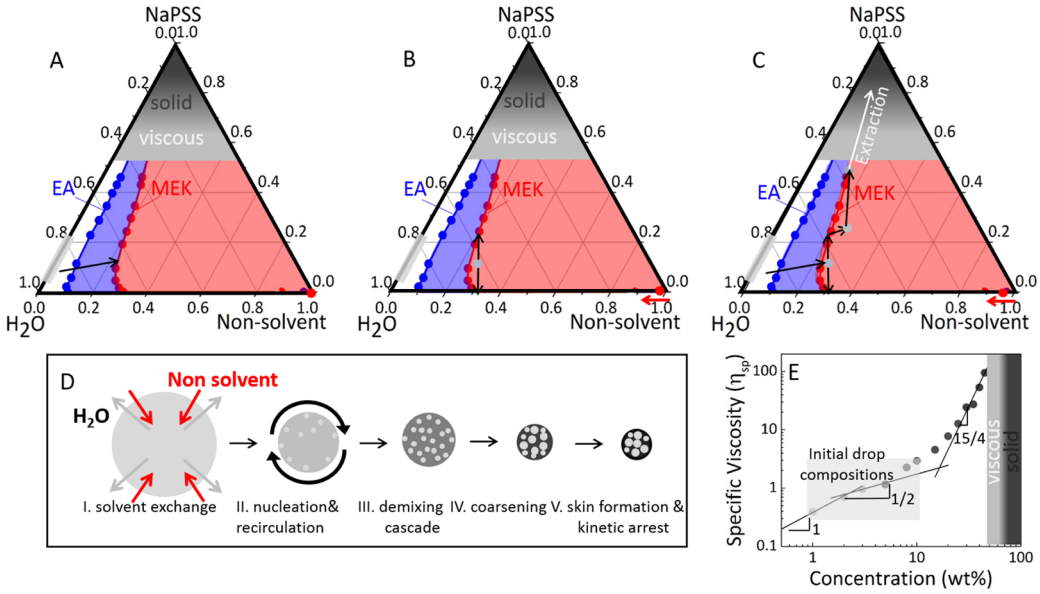

Figure 9. Proposed mechanism and pathway for porous particle formation as a function of nonsolvent quality. (A) The NaPSS/H_2O droplet composition range is indicated in gray, as is the H_2O miscibility in nonsolvent MEK. (B) Upon immersion in the nonsolvent, the droplet shrinks, increasing the polymer concentration; the ingress of nonsolvent into the droplet induces phase separation. (C) Continued droplet shrinkage further increases the polymer concentration, inducing a cascade of demixing steps. Internal coarsening of phase-separated domains continues until the concentration in the polymer-rich phases increases, eventually arresting the particle morphology, whereas the particle surface remains smooth. (D) Schematic of a polymer solution droplet during solvent extraction as indicated in A–C. (E) Specific viscosities of aqueous solutions of NaPSS/H_2O as a function of concentration.

polymer solution droplet, its polymer content, and the purity of the nonsolvent bath. The results generally demonstrate that this method enables exceptional control of particle size and microporosity, without resorting to conventional porogens or complex synthetic routes. We find that, trivially, larger polymer solution droplets result in larger polymer particles. However, the ratio of particle to droplet size depends clearly on the location of the ternary phase diagram, with particles precipitated in MEK being approximately 20% larger than those formed in EA. Because the polymer content in the particle is fixed by (i) the polymer/solution droplet and (ii) initial droplet size, the nonsolvent must also impact the internal porous structure of the particles. The changes in porosity are remarkable: particles formed in EA exhibit considerably smaller pores (~1–5 μm diameter) with a narrower distribution than those formed in MEK (up to 100 μm). In both cases, the porosity can be tuned by adjusting the polymer content in the initial droplet, with lower contents evidently yielding larger porosities. Polymer capsule formation is approached in MEK by reducing the polymer content ($\leq$1%) and increasing the droplet size. The internal porosity must therefore be set by more than the location of the phase boundaries, in agreement with previous observations in membranes.[34] Indeed, the time allowed for the coarsening of the demixed droplet during solvent extraction, and before kinetic arrest, must play an important role in setting the particle microstructure. These results are, however, surprising: the extraction times are, on average, 3 times longer in EA than in MEK. One could therefore expect that further coarsening might take place during EA extraction, thus resulting in a more porous structure. The experimental observations show the reverse, which we interpret in terms of the interplay between extraction kinetics and outer polymer crust formation, slowing down further solvent removal. The solubility of water in EA and MEK is, respectively, 3 and 11 v/v %, and the ternary miscibility boundary roughly follows this water/nonsolvent fraction in approximately the same ratio as for the extraction times. This correlation is significant because it suggests that nonsolvent quality is an effective means to tune extraction kinetics (and that, in these systems, neat solvent miscibilities provide good estimates for the ternary system).

We show that the deeper quench experienced by the polymer solution in EA, with the lower miscibility, results in initially smaller phase sizes and stronger phase segregation (viz., polymer enrichment in the polymer-rich phase); in turn, the viscosity of this phase increases, which slows down coarsening. Despite the longer EA extraction time, these particles are able to retain small pore sizes (corresponding to the polymer-poor phase) before solidification occurs, leading to the completion of the external polymer film.

The formation of microporous polymer particles along this route is thus distinct from the formation of polymer membranes by phase inversion or other directional solidification processes that emanate from the interface.[20,21] In our case, the compact and smooth outer polymer membrane forms only at the end of the particle formation process (Supporting Information movies S1 and S2), whereas polymer-poor droplets nucleate as a result of solvent exchange at the interface during extraction. Droplet flow recirculation redistributes the demixed phase: convection, in addition to diffusion, defines, to a great extent, the internal droplet structure.

The overall mechanism, kinetics, and pathway thus depend nontrivially on the ternary miscibility, solvent exchange kinetics, and time scale associated with internal droplet coalescence and recirculation. Despite this complexity, our article demonstrates that fine control can be exerted in particle size and microporosity and rationalized in terms of well-defined processes, suggesting promising routes for porous microparticles by further addition of components (e.g., polymers, copolymers, nano/microparticles, and surfactants) or coupling

DOI: 10.1021/acs.langmuir.6b01799
Langmuir 2016, 32, 8131–8140

with external fields (e.g., flow, droplet confinement, and temperature).

■ ASSOCIATED CONTENT

Supporting Information

The Supporting Information is available free of charge on the ACS Publications website at DOI: 10.1021/acs.langmuir.6b01799.

Video depicting the mechanism and kinetics of solvent extraction of 1.0 wt % NaPSS/H_2O in neat MEK on a time scale of 80 s (AVI)

Video depicting the mechanism and kinetics of solvent extraction of 1.0 wt % NaPSS/H_2O in neat EA on a time scale of 290 s (AVI)

Microfluidic device fabrication, descriptions of optical microscopy movies illustrating droplet extraction kinetics, droplet extraction with MEK and with H_2O-diluted MEK, additional SEM images of MEK-extracted particles, and additional data analysis on droplet kinetics (PDF). Data is available on request: please contact polymer-microfluidics@imperial.ac.uk.

■ AUTHOR INFORMATION

Corresponding Author

*E-mail: j.cabral@imperial.ac.uk.

Notes

The authors declare no competing financial interest.

■ ACKNOWLEDGMENTS

C.E.U. thanks the Department of Chemical Engineering, Imperial College London for a Ph.D. studentship. We thank the Engineering and Physical Sciences Research Council (EPSRC) for financial support (EP/L020564/1). Financial support under the Seventh Framework Programme of the European Commission (grant agreement no. 618333) is also acknowledged. The Institut Laue-Langevin, Grenoble, France is gratefully acknowledged for beam time, and Lionel Porcar is thanked for assistance during SANS experiments. We thank Carlos Gonzalez Lopez, Takaichi Watanabe, and Brandon Vogel for useful discussions on microfluidic extraction.

■ REFERENCES

(1) Kumacheva, E.; Garstecki, P. *Microfluidic Reactors for Polymer Particles*; John Wiley & Sons: Oxford, U.K., 2011.

(2) Berkland, C.; Kim, K. K.; Pack, D. W. Fabrication of PLG microspheres with precisely controlled and monodisperse size distributions. *J. Controlled Release* **2001**, *73*, 59−74.

(3) Berkland, C.; King, M.; Cox, A.; Kim, K. K.; Pack, D. W. Precise control of PLG microsphere size provides enhanced control of drug release rate. *J. Controlled Release* **2002**, *82*, 137−147.

(4) Vehring, R.; Foss, W. R.; Lechuga-Ballesteros, D. Particle formation in spray drying. *J. Aerosol Sci.* **2007**, *38*, 728−746.

(5) Gokmen, M. T.; Du Prez, F. E. Porous polymer particles: A comprehensive guide to synthesis, characterization, functionalization and applications. *Prog. Polym. Sci.* **2012**, *37*, 365−405.

(6) Shah, R. K.; Shum, H. C.; Rowat, A. C.; Lee, D.; Agresti, J. J.; Utada, A. S.; Chu, L.-Y.; Kim, J.-W.; Fernandez-Nieves, A.; Martinez, C. J.; Weitz, D. A. Designer emulsions using microfluidics. *Mater. Today* **2008**, *11*, 18−27.

(7) Wan, J.; Bick, A.; Sullivan, M.; Stone, H. A. Controllable microfluidic production of microbubbles in water-in-oil emulsions and the formation of porous microparticles. *Adv. Mater.* **2008**, *20*, 3314−3318.

(8) Watanabe, T.; Lopez, C. G.; Douglas, J. F.; Ono, T.; Cabral, J. T. Microfluidic Approach to the Formation of Internally Porous Polymer Particles by Solvent Extraction. *Langmuir* **2014**, *30*, 2470−2479.

(9) Yang, J.; Katagiri, D.; Mao, S.; Zeng, H.; Nakajima, H.; Uchiyama, K. Generation of controlled monodisperse porous polymer particles by dipped inkjet injection. *RSC Adv.* **2015**, *5*, 7297−7303.

(10) Shum, H. C.; Abate, A. R.; Lee, D.; Studart, A. R.; Wang, B.; Chen, C.-H.; Thiele, J.; Shah, R. K.; Krummel, A.; Weitz, D. A. Droplet Microfluidics for Fabrication of Non-Spherical Particles. *Macromol. Rapid Commun.* **2010**, *31*, 108−118.

(11) Zhang, H.; Ju, X.-J.; Xie, R.; Cheng, C.-J.; Ren, P.-W.; Chu, L.-Y. A microfluidic approach to fabricate monodisperse hollow or porous poly(HEMA-MMA) microspheres using single emulsions as templates. *J. Colloid Interface Sci.* **2009**, *336*, 235−43.

(12) Vauthier, C.; Bouchemal, K. Methods for the Preparation and Manufacture of Polymeric Nanoparticles. *Pharm. Res.* **2009**, *26*, 1025−1058.

(13) Rao, J. P.; Geckeler, K. E. Polymer nanoparticles: Preparation techniques and size-control parameters. *Prog. Polym. Sci.* **2011**, *36*, 887−913.

(14) Fessi, H.; Puisieux, F.; Devissaguet, J.; Ammoury, N.; Benita, S. Nanocapsule formation by interfacial polymer deposition following solvent displacement. *Int. J. Pharm.* **1989**, *55*, R1−R4.

(15) Zhang, C.; Pansare, V. J.; Prud'homme, R. K.; Priestley, R. D. Flash nanoprecipitation of polystyrenenanoparticles. *Soft Matter* **2012**, *8*, 86−93.

(16) Lim, J.-M.; Swami, A.; Gilson, L. M.; Chopra, S.; Choi, S.; Wu, J.; Langer, R.; Karnik, R.; Farokhzad, O. C. Ultra-high throughput synthesis of nanoparticles with homogeneous size distribution using a coaxial turbulent jet mixer. *ACS Nano* **2014**, *8*, 6056−65.

(17) Dou, S.; Colby, R. H. Solution Rheology of a Strongly Charged Polyelectrolyte in Good Solvent. *Macromolecules* **2008**, *41*, 6505−6510.

(18) Cabral, J. T.; Hudson, S. D.; Harrison, C.; Douglas, J. F. Frontal Photopolymerization for Microfluidic Applications. *Langmuir* **2004**, *20*, 10020−10029.

(19) Harrison, C.; Cabral, J. T.; Stafford, C. M.; Karim, A.; Amis, E. J. A rapid prototyping technique for the fabrication of solvent-resistant structures. *J. Micromech. Microeng.* **2004**, *14*, 153−158.

(20) Strathmann, H.; Kock, K. The formation mechanism of phase inversion membranes. *Desalination* **1977**, *21*, 241−255.

(21) Smolders, C.; Reuvers, A.; Boom, R.; Wienk, I. Microstructures in phase-inversion membranes. Part 1. Formation of macrovoids. *J. Membr. Sci.* **1992**, *73*, 259−275.

(22) Akbulut, M.; Ginart, P.; Gindy, M. E.; Theriault, C.; Chin, K. H.; Soboyejo, W.; Prud'homme, R. K. Generic Method of Preparing Multifunctional Fluorescent Nanoparticles Using Flash NanoPrecipitation. *Adv. Funct. Mater.* **2009**, *19*, 718−725.

(23) Hayter, J.; Janninck, G.; Brochard-Wyart, F.; De Gennes, P. Correlations and dynamics of polyelectrolyte solutions. *J. Phys., Lett.* **1980**, *41*, 451−454.

(24) Lopez, C. G.; Rogers, S. E.; Colby, R. H.; Graham, P.; Cabral, J. T. Structure of Sodium Carboxymethyl Cellulose Aqueous Solutions: A SANS and Rheology Study. *J. Polym. Sci., Part B: Polym. Phys.* **2015**, *53*, 492−501.

(25) De Gennes, P.; Pincus, P.; Velasco, R.; Brochard, F. Remarks on polyelectrolyte conformation. *J. Phys. (Paris)* **1976**, *37*, 1461−1473.

(26) Nierlich, M.; Williams, C.; Boué, F.; Cotton, J.; Daoud, M.; Famoux, B.; Jannink, C.; Moan, M.; Wolff, C. Small angle neutron scattering by semi-dilute solutions of polyelectrolyte. *J. Phys. (Paris)* **1979**, *40*, 701−704.

(27) Nishida, K.; Kaji, K.; Kanaya, T.; Shibano, T. Added Salt Effect on the Intermolecular Correlation in Flexible Polyelectrolyte Solutions: Small-Angle Scattering Study. *Macromolecules* **2002**, *35*, 4084−4089.

(28) Spiteri, M. N.; Williams, C. E.; Boué, F. Pearl-Necklace-Like Chain Conformation of Hydrophobic Polyelectrolyte: a SANS Study of Partially Sulfonated Polystyrene in Water. *Macromolecules* **2007**, *40*, 6679−6691.

DOI: 10.1021/acs.langmuir.6b01799
Langmuir 2016, 32, 8131−8140

(29) Higgins, J. S.; Benoit, H. C. *Polymers and Neutron Scattering*; Oxford University Press, Inc, 1994.
(30) Pedersen, J. S.; Rennie, A.; Glatter, O.; Naudon, A.; Schmidt, P. et al., In *Modern Aspects of Small-Angle Scattering*; Brumberger, H., Ed.; Springer Science, 1995; pp 273−303.
(31) Duncan, P. B.; Needham, D. Microdroplet dissolution into a second-phase solvent using a micropipet technique: Test of the epstein-plesset model for an aniline-water system. *Langmuir* **2006**, *22*, 4190−4197.
(32) Tsay, C. S.; McHugh, A. J. The combined effects of evaporation and quench steps on asymmetric membrane formation by phase inversion. *J. Polym. Sci., Part B: Polym. Phys.* **1991**, *29*, 1261−1270.
(33) Dobrynin, A.; Rubinstein, M. Theory of polyelectrolytes in solutions and at surfaces. *Prog. Polym. Sci.* **2005**, *30*, 1049−1118.
(34) Barton, B. F.; Reeve, J. L.; McHugh, A. J. Observations on the dynamics of nonsolvent-induced phase inversion. *J. Polym. Sci., Part B: Polym. Phys.* **1997**, *35*, 569−585.

DOI: 10.1021/acs.langmuir.6b01799
Langmuir 2016, 32, 8131−8140